Supplemental material

Supplemental methods

Image processing pipeline for heart–torso model construction from clinical MRI data

The novel image processing pipeline for heart-torso model construction from clinical MRI data is described in the main text, with additional detail provided here. After manual labelling and interpolation into 1 mm resolution as was described in the Methods section, the interpolated images were merged into one image. During this merging, whenever voxels corresponding to the whole torso region overlapped with those corresponding to any of the other regions, the former were replaced with the latter. Next, the merged image was modified by labelling the remaining voxels in the torso as conductive medium. If the acquired patient MRI image does not extend into the abdomen (as was the case with the tricuspid valve atresia patient dataset in this study), additional slices marked as conductive medium can be added to the abdominal side. This is done in order to extend the dimensions of the torso model so as to be able to incorporate additional abdominal implantable cardioverter–defibrillator (ICD) can positions. Twelve slices were added here.

After segmentation of the ventricle, merging of the ventricle with the torso image, and generation of the computational mesh as described in the Methods section, region identifiers from the torso image were automatically assigned to the elements, thereby differentiating the elements that belonged to different tissue types.

Model formulation and parameters

The mathematical description of current flow in cardiac tissue was based on the bidomain representation (Plonsey, 1988), which can be simplified into the monodomain representation for all instants after the shock. In order to preserve the same conduction velocities (CVs) and propagation patterns between the monodomain and bidomain simulations, we used the harmonic mean conductivity (g_m) as the monodomain conductivity with $g_{m,\zeta} = \frac{g_{i,\zeta} g_{e,\zeta}}{g_{i,\zeta} + g_{e,\zeta}}$, where g_i is the bidomain intracellular conductivity and g_e

the bidomain extracellular conductivity, and ζ represents longitudinal, transverse, or sheet-normal fibre direction (Bishop & Plank, 2011).

The bidomain and monodomain equations were solved with the Cardiac Arrhythmia Research Package (CARP) (Vigmond *et al.*, 2002; Vigmond *et al.*, 2003). The numerical techniques used in CARP have been described elsewhere (Plank *et al.*, 2007; Plank *et al.*, 2008; Vigmond *et al.*, 2008), a brief description follows. The bidomain formulation (Plonsey, 1988) was recast using an operator splitting approach, which yields:

$$\nabla \cdot (\bar{\sigma}_i + \bar{\sigma}_e)\nabla\Phi_e = -\nabla \cdot \bar{\sigma}_i \nabla V_m - I_e$$

$$\nabla \cdot \bar{\sigma}_i \nabla V_m = -\nabla \cdot \bar{\sigma}_i \nabla\Phi_e + \beta I_m \quad .$$

Here, $\bar{\sigma}_i$ and $\bar{\sigma}_e$ are the intra- and extracellular conductivity tensors, Φ_e is the extracellular potential, V_m the transmembrane potential, I_e the extracellular current stimulus, β the surface to volume ratio of cardiac cells, and I_m the transmembrane current density. The first equation is an elliptic problem, the second equation is a parabolic problem, which are solved separately. After discretization, a linear system is solved at every time step using an iterative approach with a preconditioned conjugate gradient (Vigmond *et al.*, 2008). In the monodomain case, only the equation $\nabla \cdot \bar{\sigma}_m \nabla V_m = I_m$ needed to be solved, where $\bar{\sigma}_m$ is the harmonic mean conductivity tensor. The monodomain case was solved similarly to the bidomain, but using the equation with harmonic mean conductivity values. With this bidomain–monodomain approach, simulating, using the bidomain approach, a 7 ms shock with time steps of 0.5 μs took less than five hours, while simulating 1 s of post-shock propagation, in monodomain mode, with time steps of 5 μs took less than nine hours on eight nodes (64 cores) on an IBM iDataPlex Linux cluster. Each node on the cluster has dual Intel Xeon Quad Core E5472 3.00 GHz processors and 32 GB random-access memory (RAM). The cluster is connected via 4× double data rate (DDR) InfiniBand fabric and utilizes IBM's general parallel file system (GPFS). The number of elements of the tricuspid valve atresia heart–torso mesh is shown in Figure 1.

Ionic properties of cardiac myocytes were modelled with the ten Tusscher model of the human ventricular myocyte (ten Tusscher & Panfilov, 2006). A 40 % apico–basal gradient in the maximal conductance of the slowly activating component of the delayed rectifier current (I_{Ks}) was implemented (Szentadrassy *et al.*, 2005; Okada *et al.*, 2011). The ventricular wall was divided equally into endocardial, midmyocardial, and epicardial cell layers, and the maximum conductances of the transient outward (I_{to}) and I_{Ks} potassium channels were adjusted to represent realistic transmural electrophysiological heterogeneity (Glukhov *et al.*, 2010; Moreno *et al.*, 2011). In order to make the simulated action potential duration (APD) similar to the *QT* interval of the patient's ECG (Fig. 3), G_{Ks} was increased, decreasing APD. The values of G_{to} and G_{Ks} are given in Supplemental Table S1.

Supplemental Table S1: Parameter values used in the ventricular model. G_{to}, I_{to} maximum conductance; G_{Ks}, I_{Ks} maximum conductance; $g_{i,l}$, intracellular longitudinal conductivity; $g_{i,t}$, intracellular transverse conductivity; $g_{i,n}$, intracellular sheet-normal conductivity; $g_{e,l}$, extracellular longitudinal conductivity; $g_{e,t}$, extracellular transverse conductivity; $g_{e,n}$, extracellular sheet-normal conductivity;

Parameters	Endocardium	Midmyocardium	Epicardium
G_{to} [nS pF^{-1}]	0.073	0.294	0.294
G_{Ks} [nS pF^{-1}]	0.245	0.6125	0.98
$g_{i,l}$ [S m^{-1}]	1.15	1.15	0.442
$g_{i,t}$ [S m^{-1}]	0.247	0.247	0.124
$g_{i,n}$ [S m^{-1}]	0.086	0.086	0.053
$g_{e,l}$ [S m^{-1}]	1.15	1.15	1.15
$g_{e,t}$ [S m^{-1}]	0.46	0.46	0.46
$g_{e,n}$ [S m^{-1}]	0.46	0.46	0.46

Ventricular conductivities were chosen to achieve realistic activation patterns, achieving the experimentally observed ratio of 4:1.8:1 between longitudinal, transverse, and sheet-normal CVs (Caldwell *et al.*, 2009). Epicardial conductivities were reduced in order to achieve a 30 % reduction in epicardial CV (Poelzing *et al.*, 2004). The conductivities used in this study are given in Supplemental Table S1. As stated in the Methods section, tissue conductivities were assigned the values used by Jolley *et al.* (2008). Our "conductive medium" tissue type corresponded to their "connective tissue" type (with a conductivity of 0.22 S m^{-1}). We used "conductive medium" because "connective tissue" could imply insulating properties. Skin was assigned the same "connective tissue" conductivity, as skin was not specifically segmented in the study by Jolley *et al.* (2008) and, hence, no separate conductivity values were given for skin.

Electrocardiogram computation

The nine standard ECG electrodes were placed on the surface of the model torso (Suppl. Fig. S1). The left leg (*LL*) electrode, as positioned in the model torso, is much closer to the heart than in a clinical ECG electrode location, due to the limited size of the torso (as per the original MRI scans). To evaluate a more realistic *LL* electrode position as well, an alternative *LL* electrode was placed at a position more inferior to the torso mesh ("far *LL*") to better resemble the clinical position of a *LL* electrode. Fundamentally, the ECG was determined in two different ways: 1) calculating the ECG using the extracellular potential (Φ_e) from the bidomain simulations, or 2) determining the pseudo-ECG after solving the monodomain or bidomain equations by computing pseudo-Φ_e using the recovery technique as described by Gima and Rudy (2002); the latter is based on the simplifying assumption that the ventricle is surrounded by an infinite amount of conductive medium. The advantage of the pseudo-Φ_e approach is that while it can be used in conjunction with bidomain simulations, it can also be used in conjunction with the computationally less demanding monodomain simulations, speeding up the ECG computations significantly. Pseudo-Φ_e ECGs were computed using both monodomain and bidomain formulations, and the results compared. Overall, ECGs were computed using four approaches, two of which used direct calculation of bidomain Φ_e, and two used calculation of pseudo-Φ_e: 1) direct calculation of bidomain Φ_e from the ECG electrodes shown in Supplemental Figure S1 ("ECG"/black traces in Suppl. Figs. S4, S5), 2) direct calculation of bidomain Φ_e from the ECG electrodes shown in Supplemental Figure S1, except in the case of the *LL* electrode, where pseudo-Φ_e was used instead for the more realistically positioned "far *LL*" electrode ("ECG far LL"/red traces in Suppl. Figs. S4, S5), 3) bidomain pseudo-Φ_e from the ECG electrodes shown in Supplemental Figure S1, except in the case of the *LL* electrode, where the "far *LL*" electrode was used ("pECG"/green traces in Suppl. Figs. S4, S5), and 4) monodomain pseudo-Φ_e from the ECG electrodes shown in Supplemental Figure S1, except in the case of the *LL* electrode, where the "far *LL*" electrode was used ("pECG mono"/blue traces in Suppl. Figs. S4, S5). Because the model lacked a representation of the atria, the *P* wave was absent from the simulated ECGs.

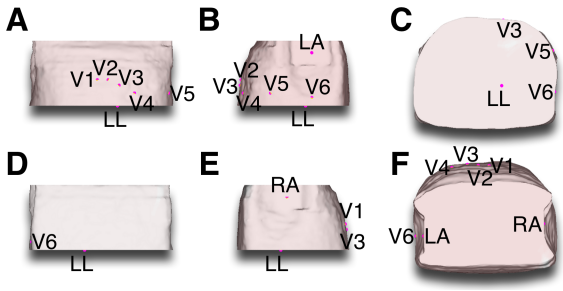

Supplemental Figure S1: Pink spheres mark ECG electrode placement locations. **A:** antero–posterior view. **B:** Left lateral view. **C:** Infero–superior view. **D:** Postero–anterior view. **E:** Right lateral view. **F:** Supero–inferior view.

Purkinje System (PS) activation in response to His bundle stimulation was simulated in a cable-based representation of the PS (Suppl. Fig. S2A). Sinus rhythm was then simulated by pacing the ventricular model from the locations of Purkinje–myocardial junctions (Suppl. Fig. S2A), where junctional activation times from the PS cable model were used as pacing offsets from t = 0. In the absence of a way to derive the PS from the patient MRI scans, the PS was derived from the left fascicles of a rabbit PS representation (Vigmond & Clements, 2007), to which affine transformations were applied to achieve conformal geometry to the patient heart in the present model. Electric propagation and Purkinje–myocardial junctional dynamics in the PS were modelled as previously described by Boyle *et al.* (2010).

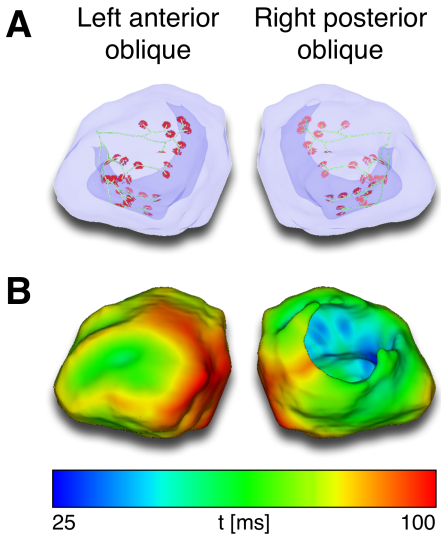

Supplemental Figure S2: A: The cable-based Purkinje system is shown in green. The ventricle is shown in transparent blue, and the pacing sites at the Purkinje–myocardial junctions are shown in red. **B:** Sinus rhythm activation maps. Ventricular activation originated at the Purkinje–myocardial junction pacing sites.

Study protocol

Ventricular fibrillation (VF) could not be induced in this model without changing the restitution properties of the ten Tusscher human ventricular ionic model (ten Tusscher & Panfilov, 2006). Therefore, some parameters in the ionic model were altered in order to increase the maximum steepness of the restitution curves (Suppl. Tab. S2 & Suppl. Fig. S3; cf. Tab. 2 in ten Tusscher and Panfilov (2006)). Sustained VF was then induced by burst pacing from the apex. Sustained ventricular tachycardia (VT) was inducible using the original ionic model (model parameters are given in the Model formulation and parameters subsection above) by the application of an ICD shock to the ventricle in sinus rhythm.

Supplemental Table S2: Parameter values used in the original human ventricular ionic model and in the model that was altered to achieve steeper restitution properties (cf. Tab. 2 in ten Tusscher and Panfilov (2006)). G_{Ks}, I_{Ks} maximum conductance, G_{Kr}, I_{Kr} maximum conductance, G_{pCa}, I_{pCa} maximum conductance, G_{pK}, I_{pK} maximum conductance, τ_f inact , multiplication factor for voltages > 0 mV for the time constant of the *f* gate;

Parameters	**Original model**	**Altered model**
G_{Ks} endocardium [nS pF^{-1}]	0.245	0.3101
G_{Ks} midmyocardium [nS pF^{-1}]	0.6125	0.7752
G_{Ks} epicardium [nS pF^{-1}]	0.98	1.2403
G_{Kr} [nS pF^{-1}]	0.153	0.1934
G_{pCa} [nS pF^{-1}]	0.1238	6.0662
G_{pK} [nS pF^{-1}]	0.0146	0.0003
τ_f inact	× 1	× 4

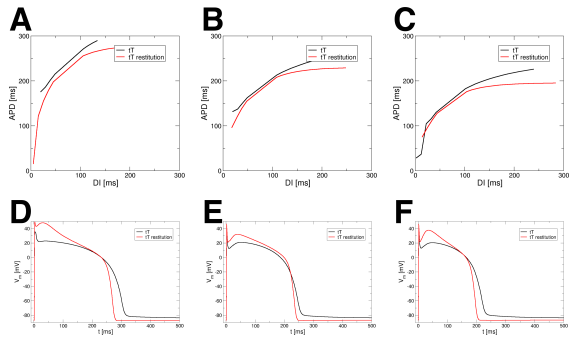

Supplemental Figure S3: **A:** Endocardial S1–S2 restitution curves for the original ten Tusscher human ventricular ionic model (black; "tT") and the altered model (red; "tT restitution"). Note the increased maximum slope of the restitution curve in the altered ionic model. **B:** Mid-myocardial S1–S2 restitution curves. **C:** Epicardial S1–S2 restitution curves. **D:** Endocardial action potentials for the original human ionic model and the altered model, paced at 500 ms pacing cycle length. The APD is shorter in the altered model. **E:** Mid-myocardial action potentials. **F:** Epicardial action potentials.

In order to construct defibrillation threshold (DFT) and cardioversion threshold (CVT) grids, defibrillation and cardioversion shocks were applied starting at 80 J. Shock energy was calculated as $E = \frac{V^2}{R}t$, where E is shock energy, V is shock voltage, R is the shock vector-specific bulk resistance of the heart–torso model, and t is the duration of the shock. If the initial shock successfully terminated the arrhythmia, the shock energy was halved until the termination attempt was unsuccessful and the threshold was found; if the initial shock did not terminate the arrhythmia, shock energy was doubled until arrhythmia was terminated and the DFT or CVT was found.

The VF and VT cycle lengths (CLs) were defined as the inverse of the median dominant frequency (DF). The DF was computed over multiple seconds of VF or VT for every node in the ventricular mesh by constructing a Fast Fourier Transformation of transmembrane potential (V_m) in time and then determining the frequency that corresponded to the largest magnitude in the frequency spectrum.

Φ_e gradients were calculated at every node in the ventricular mesh. The mean Φ_e gradient associated with a particular ICD configuration and shock strength was then calculated from these nodal Φ_e gradients. The Φ_e gradients were compared between groups of ICD configurations by using mean ± standard deviation, where group mean and standard deviation were taken over the individual ICD configurations' means.

Supplemental results

The electrocardiogram

The second ECG computation method mentioned in the Supplemental methods section above, namely calculating the bidomain Φ_e at the locations of the ECG electrodes on the torso model surface (Suppl. Fig. S1), except in the case of the *LL* electrode, where pseudo-Φ_e was used at the more realistically positioned "far *LL*" electrode instead ("ECG far LL"/red traces in Suppl. Figs. S4, S5), matched the patient's clinical ECG recordings most closely (Suppl. Figs. S4, S5). Using this ECG computation method, the simulated *QRS* complex polarity matched the clinical in all limb lead recordings, in all augmented limb leads (Suppl. Fig. S4), and in two of the precordial leads (*V1*, *V2*; Suppl. Fig. S5). The *T* wave polarity matched in two limb leads (*I*, *III*), two augmented limb leads (*aVR*, *aVL*; Suppl. Fig. S4), and in all precordial lead recordings (Suppl. Fig. S5). Since the PS could not be reconstructed specifically for this patient, but a generic PS representation had to be used, it was not to be expected that the simulated ECG and the clinical ECG recording would be perfect matches in all leads. Nevertheless, the achieved polarity matches showed that the developed heart–torso model was an appropriate representation of the patient's electrophysiology. ECG signal amplitudes were generally larger in the simulated ECGs than in the clinical ones, regardless of the ECG computation method used.

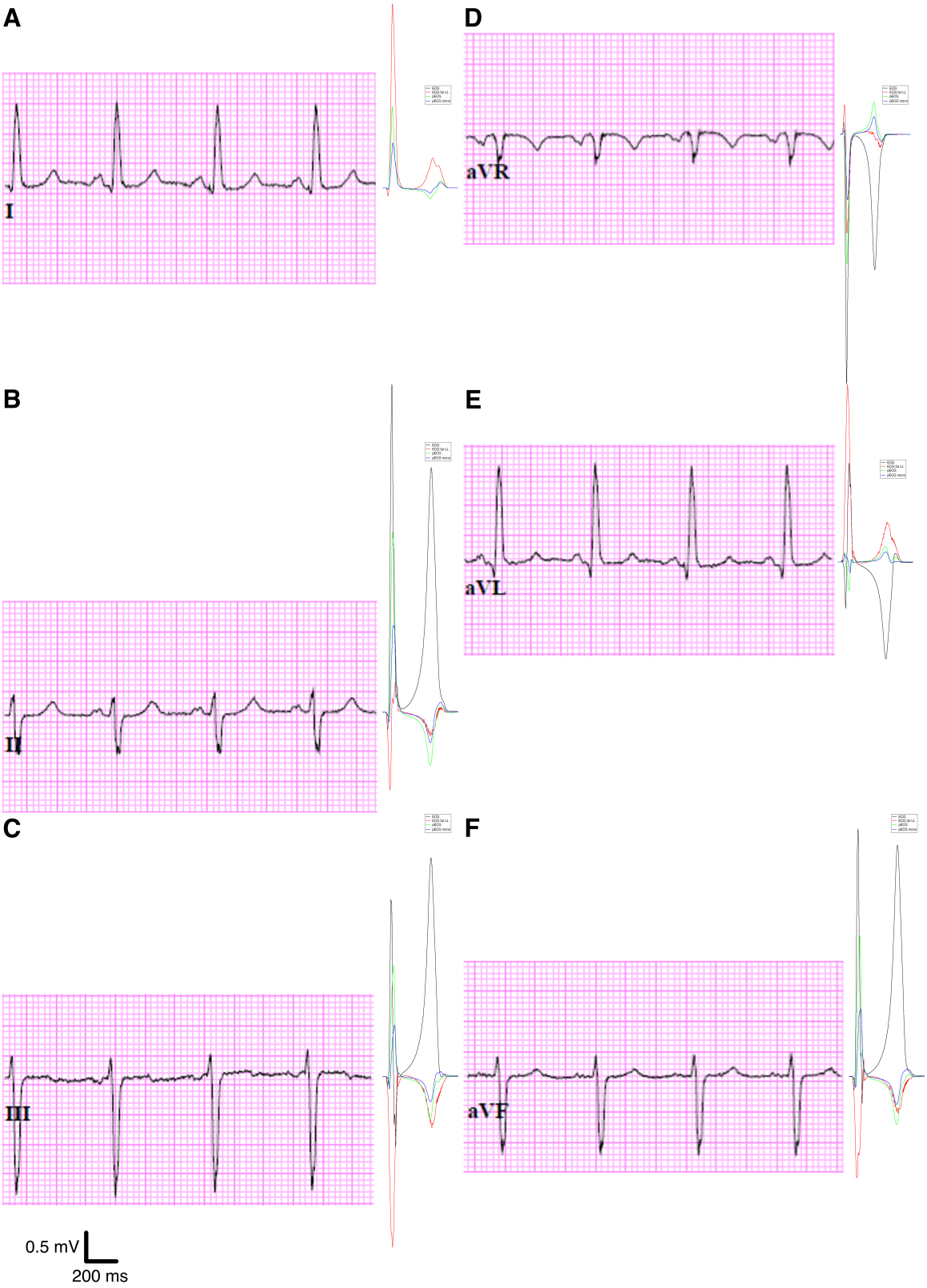
A
I
D
aVR
B
II
E
aVL
C
III
F
aVF
0.5 mV
200 ms

Supplemental Figure S4: Clinical (left panels) and simulated (right panels) limb and augmented limb lead ECG traces of the paediatric tricuspid valve atresia patient. For the modelled traces, ECGs computed from bidomain Φ_e values are shown in black, ECGs computed from bidomain Φ_e values except for the *LL* electrode, which is taken from a far-field pseudo-Φ_e value, are shown in red, pseudo-ECGs computed from pseudo-Φ_e of bidomain simulations are shown in green, and pseudo-ECGs computed from pseudo-Φ_e from monodomain simulations are shown in blue. **A:** Lead *I*. **B:** Lead *II*. **C:** Lead *III*. **D:** Lead *aVR*. **E:** Lead *aVL*. **F:** Lead *aVF*.

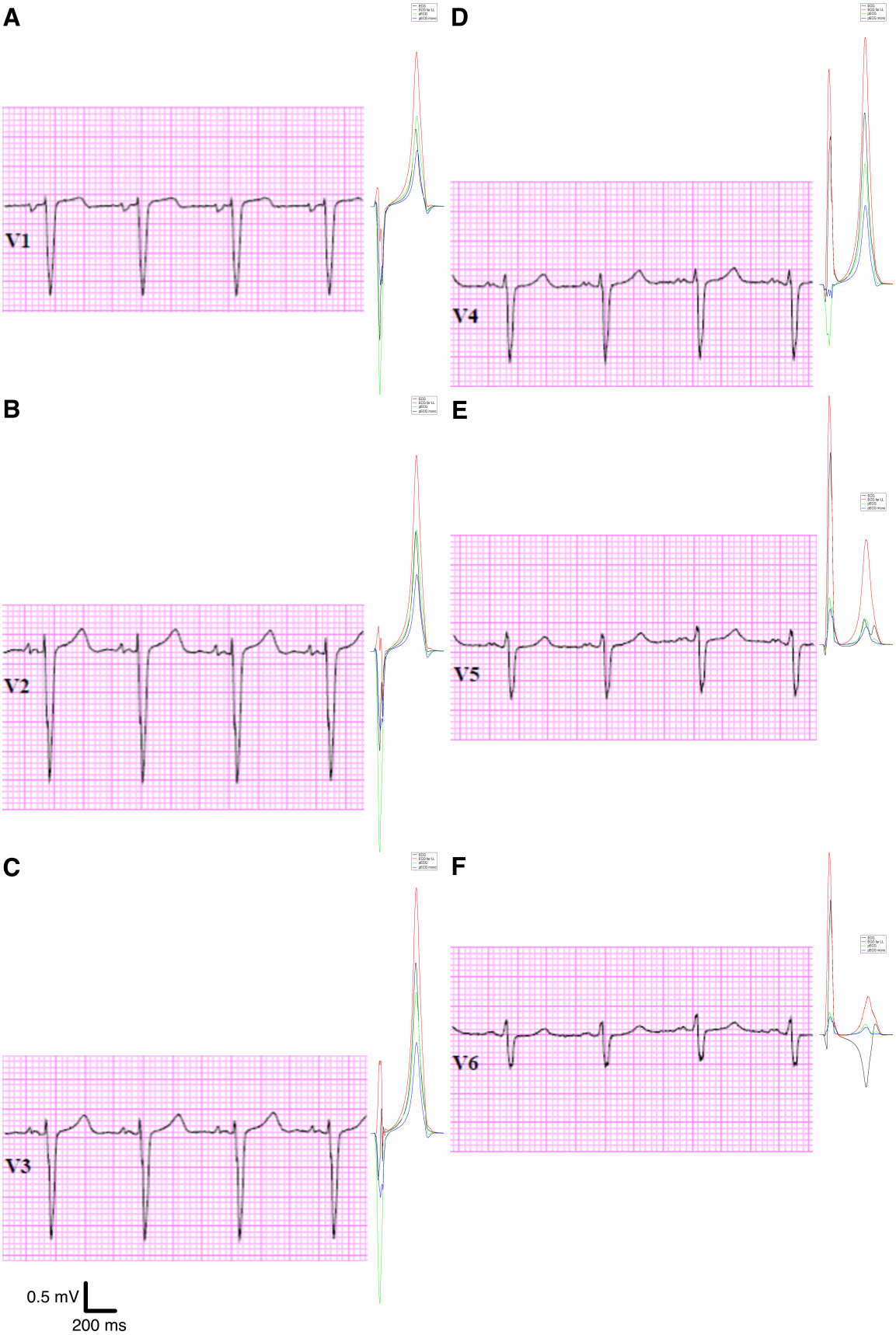
A
V1
B
V2
C
V3
D
V4
E
V5
F
V6
0.5 mV
200 ms

Supplemental Figure S5: Clinical (left panels) and simulated (right panels) precordial lead ECG traces of the paediatric tricuspid valve atresia patient. Colours of the simulated traces are the same as in Supplemental Figure S4. **A:** Lead *V1*. **B:** Lead *V2*. **C:** Lead *V3*. **D:** Lead *V4*. **E:** Lead *V5*. **F:** Lead *V6*.

Our simulations demonstrate that pseudo-ECG traces were very similar when pseudo-Φ_e was reconstructed from bidomain simulations ("pECG"/green traces in Suppl. Figs. S4, S5; third ECG computation method in Supplemental methods) and monodomain simulations ("pECG mono"/blue traces in Suppl. Figs. S4, S5; fourth ECG computation method in Supplemental methods). While the signal amplitudes differed, *QRS* complex and *T* wave polarities were identical for mono- and bidomain pseudo-ECGs for all 12 leads, as were the timings of wave onsets, peaks, and ends. This suggested that propagation patterns and recovery times were very similar between monodomain and bidomain simulations. These results further validated our strategy of using the monodomain formulation to simulate pre- and post-shock propagation, and only using the bidomain approach when applying an external electric field (i.e., a far-field electric shock).

Ventricular fibrillation and ventricular tachycardia

The VF median DF was 6.10074 Hz, corresponding to a VF CL of 164 ms, whereas the VT median DF was 3.66692 Hz, corresponding to a VT CL of 273 ms. The three instants of time at which shocks were given (i.e., the pre-shock phases of VT or VF) were equally distributed within one arrhythmia "cycle", i.e. were spaced ⅓ CL apart from each other. In this way, three different pre-shock V_m distributions associated with VF or VT would be subjected to defibrillation or cardioversion shocks. Thus, VF phases were 55 ms apart, while VT phases were 91 ms apart. The phases were chosen after the induced VF and VT had been allowed to persist for several seconds. DF histograms and boxplots of the VF and VT episodes are shown in Supplemental Figure S6. Figure 4 in the main text shows V_m maps associated with these VF and VT phases, along with 2 s excerpts of limb lead ECG recordings.

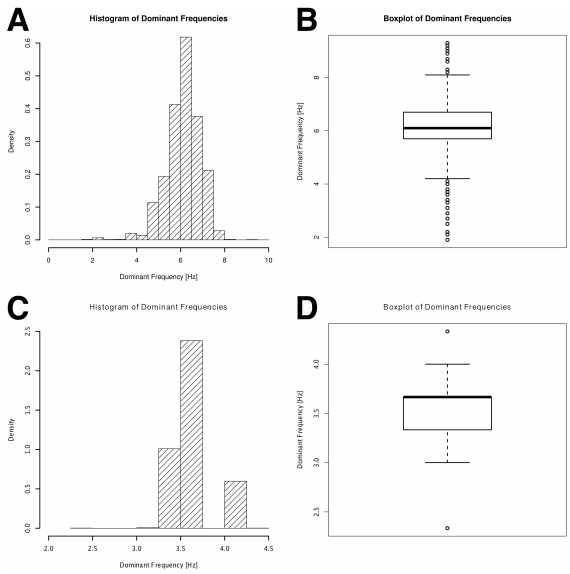

Supplemental Figure S6: A: Histogram of VF DFs. **B:** Boxplot of VF DFs. **C:** Histogram of VT DFs. **D:** Boxplot of VT DFs.

Extracellular potentials

Supplemental Table S3 shows data pertaining to Φ_e gradients 1 ms after the onset of 80 J shocks. The same Φ_e gradient distributions are shown in graphical form in Figure 7.

Supplemental Table S3: Mean, standard deviation, and median Φ_e gradients 1 ms after the onset of 80 J shocks (see also Fig. 7). Units are V cm^{-1}. ICD configuration notation as in Figure 2.

ICD configuration	Mean	Standard deviation	Median
LEpiL2RCC	20.39	20.18	15.59
PEpiL2LCC	32.59	21.64	27.95
REpiL2SCC	24.47	16.73	21.02
LSqL2RPSC	5.68	1.54	5.31
LSqL2RCC	6.07	2.33	5.47
PSqL2SCC	6.23	1.72	5.83
PSqL2LCC	10.16	3.63	8.89
LPSL2SAC	10.88	6.56	8.92
LSqLPSqLLPSL 2SCC	7.86	4.08	6.50
PSqLLPSL2SCC	8.25	4.89	6.80
PSqLLPSL2SAC	7.77	4.46	6.63

Supplemental Figure S7 shows a plot of mean Φ_e gradients 1 ms after the onset of 80 J shocks (same simulations as in Fig. 7 and Suppl. Tab. S3) against the DFTs (from Fig. 5) and CVTs (from Fig. 6) of the corresponding ICD configurations. The high Φ_e gradients observed in the ICD configurations with epicardial leads correspond to low DFTs and CVTs. However, for the lower Φ_e gradients observed in the ICD configurations with subcutaneous leads, no obvious correlation can be seen between Φ_e gradient magnitude on the one hand and DFT and CVT on the other hand.

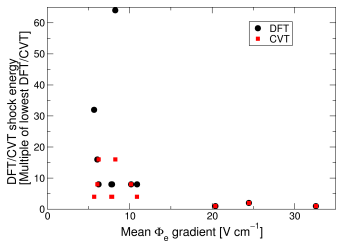

Supplemental Figure S7: Mean Φ_e gradients 1 ms after the onset of 80 J shocks plotted against the DFTs (black circles) and CVTs (red squares) of the corresponding ICD configurations. Φ_e gradients as in Figure 7 and Supplemental Table S3, DFTs as in Figure 5, CVTs as in Figure 6.

Defibrillation threshold of a submuscular ICD can configuration

Supplementary Figure S8A shows an alternative placement location for the sub-axillary can as an example of a "deeper" can placement, mimicking ICD can placement in a submuscular pocket. Supplementary Figure S8B shows the DFTs of the ICD configuration with a left para-sternal lead and a sub-axillary can (see also Figs. 2 and 5), and of an alternative ICD configuration with a left para-sternal lead and the submuscular sub-axillary can from Supplementary Figure S8A. Defibrillation outcome was the same for defibrillating at phases 1 and 2, but one defibrillation instance at phase 3 at 4 times the lowest DFT overall resulted in successful defibrillation with the "deeper" can, but not in the sub-axillary can positioned as shown in Figure 2. Hence, the overall DFT was lower for the ICD configuration mimicking ICD can placement in a submuscular pocket.

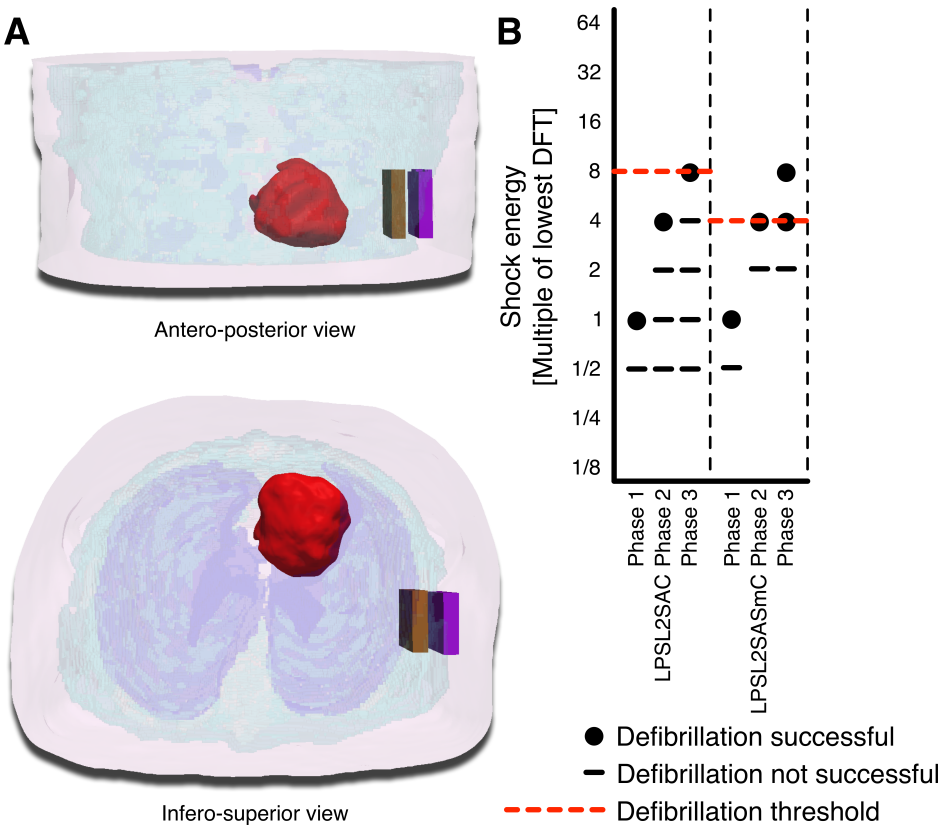

Supplemental Figure S8: A: The finite element heart–torso mesh and two sub-axillary ICD can placement locations. The purple ICD can is at the same location as the sub-axillary can in Figure 2. The brown ICD can represents a deeper location to represent ICD can placement in a submuscular pocket. The ventricles are shown in red, skin in pink transparent, bones in white transparent, lungs in blue transparent, and muscles in cyan transparent. **B:** DFTs for these two ICD configurations. Red dashed lines mark the DFTs. The left column is also shown in Figure 5. ICD configuration notation as in Figure 2 in the left column, LPSL2SASmC in the right column represents a configuration with a left para-sternal lead and the submuscular sub-axillary can from panel A. VF phases as in Figure 4.

These results suggest that placing the ICD can as deep as possible is electrically favourable for this patient. However, additional studies would be needed to confirm if the lower DFT (in VF phase 3) is due to placing the can in a deeper, submuscular location per se, or if it is rather the changed shock vector that

is electrically favourable. If the latter is the case, a right para-sternal lead instead of a left para-sternal lead could potentially have the same effect on DFT without the need for a deeper placement of the ICD can.

Supplemental References

Bishop MJ & Plank G. (2011). Representing cardiac bidomain bath-loading effects by an augmented monodomain approach: application to complex ventricular models. *IEEE Trans Biomed Eng* **58,** 1066-1075.

Boyle PM, Deo M, Plank G & Vigmond EJ. (2010). Purkinje-mediated effects in the response of quiescent ventricles to defibrillation shocks. *Ann Biomed Eng* **38,** 456-468.

Caldwell BJ, Trew ML, Sands GB, Hooks DA, LeGrice IJ & Smaill BH. (2009). Three distinct directions of intramural activation reveal nonuniform side-to-side electrical coupling of ventricular myocytes. *Circ Arrhythm Electrophysiol* **2,** 433-440.

Gima K & Rudy Y. (2002). Ionic current basis of electrocardiographic waveforms: a model study. *Circ Res* **90,** 889-896.

Glukhov AV, Fedorov VV, Lou Q, Ravikumar VK, Kalish PW, Schuessler RB, Moazami N & Efimov IR. (2010). Transmural dispersion of repolarization in failing and nonfailing human ventricle. *Circ Res* **106,** 981-991.

Jolley M, Stinstra J, Pieper S, Macleod R, Brooks DH, Cecchin F & Triedman JK. (2008). A computer modeling tool for comparing novel ICD electrode orientations in children and adults. *Heart Rhythm* **5,** 565-572.

Moreno JD, Zhu ZI, Yang PC, Bankston JR, Jeng MT, Kang C, Wang L, Bayer JD, Christini DJ, Trayanova NA, Ripplinger CM, Kass RS & Clancy CE. (2011). A computational model to

predict the effects of class I anti-arrhythmic drugs on ventricular rhythms. *Sci Transl Med* **3,** 98ra83.

Okada J, Washio T, Maehara A, Momomura S, Sugiura S & Hisada T. (2011). Transmural and apicobasal gradients in repolarization contribute to T-wave genesis in human surface ECG. *Am J Physiol Heart Circ Physiol* **301,** H200-208.

Plank G, Liebmann M, Weber dos Santos R, Vigmond EJ & Haase G. (2007). Algebraic multigrid preconditioner for the cardiac bidomain model. *IEEE Trans Biomed Eng* **54,** 585-596.

Plank G, Zhou L, Greenstein JL, Cortassa S, Winslow RL, O'Rourke B & Trayanova NA. (2008). From mitochondrial ion channels to arrhythmias in the heart: computational techniques to bridge the spatio-temporal scales. *Philos Transact A Math Phys Eng Sci* **366,** 3381-3409.

Plonsey R. (1988). Bioelectric sources arising in excitable fibers (ALZA lecture). *Ann Biomed Eng* **16,** 519-546.

Poelzing S, Akar FG, Baron E & Rosenbaum DS. (2004). Heterogeneous connexin43 expression produces electrophysiological heterogeneities across ventricular wall. *Am J Physiol Heart Circ Physiol* **286,** H2001-2009.

Szentadrassy N, Banyasz T, Biro T, Szabo G, Toth BI, Magyar J, Lazar J, Varro A, Kovacs L & Nanasi PP. (2005). Apico-basal inhomogeneity in distribution of ion channels in canine and human ventricular myocardium. *Cardiovasc Res* **65,** 851-860.

ten Tusscher KH & Panfilov AV. (2006). Alternans and spiral breakup in a human ventricular tissue model. *Am J Physiol Heart Circ Physiol* **291,** H1088-1100.

Vigmond EJ, Aguel F & Trayanova NA. (2002). Computational techniques for solving the bidomain equations in three dimensions. *IEEE Trans Biomed Eng* **49,** 1260-1269.

Vigmond EJ & Clements C. (2007). Construction of a computer model to investigate sawtooth effects in the Purkinje system. *IEEE Trans Biomed Eng* **54,** 389-399.

Vigmond EJ, Hughes M, Plank G & Leon LJ. (2003). Computational tools for modeling electrical activity in cardiac tissue. *J Electrocardiol* **36 Suppl,** 69-74.

Vigmond EJ, Weber dos Santos R, Prassl AJ, Deo M & Plank G. (2008). Solvers for the cardiac bidomain equations. *Prog Biophys Mol Biol* **96,** 3-18.